Study of the thermal stability of studtite by *in situ* Raman spectroscopy and DFT calculations

Francisco Colmenero[a*], Laura J. Bonales[b], Joaquín Cobos[b], Vicente Timón[a]

[a]Instituto de Estructura de la Materia, CSIC. C/ Serrano, 113. 28006 Madrid, Spain

[b]Centro de Investigaciones Energéticas, Medioambientales y Tecnológicas, CIEMAT. Avda/ Complutense, 40. 28040 Madrid, Spain

---

[*] Corresponding author. Tel.+34 915616800 Ext. 941033
E-mail address: francisco.colmenero@iem.cfmac.csic.es

Abstract

The design of a safe spent nuclear fuel repository requires the knowledge of the stability of the secondary phases which precipitate when water reaches the fuel surface. Studtite is recognized as one of the secondary phases that play a key-role in the mobilization of the radionuclides contained in the spent fuel. Thereby, it has been identified as a product formed under oxidation conditions at the surface of the fuel, and recently found as a corrosion product in the Fukushima-Daiichi nuclear plant accident. Thermal stability is one of the properties that should be determined due to the high temperature of the fuel.

In this work we report a detailed analysis of the structure and thermal stability of studtite. The structure has been studied both by experimental techniques (SEM, TGA, XRD and Raman spectroscopy) and theoretical DFT electronic structure and spectroscopic calculations. The comparison of the results allows us to perform for the first time the Raman bands assignment of the whole spectrum. The thermal stability of studtite has been analyzed by *in situ* Raman spectroscopy, with the aim of studying the effect of the heating rate and the presence of water. For this purpose, a new cell has been designed. The results show that studtite is stable under dry conditions only at temperatures below 30 ºC, in contrast with the higher temperatures published up to date (~ 130 ºC). Opposite behaviour has been found when studtite is in contact with water; under these conditions studtite is stable up to 90 ºC, what is consistent with the encounter of this phase after the Fukushima-Daiichi accident.

1. Introduction

Nuclear fuel, commonly composed of UO_2 pellets enriched from 0.7 to 3–5 % of ^{235}U [1], is obtained from natural minerals found in the rocks of the Earth´s crust. After its irradiation (one or more irradiation cycles) the fuel is considered as spent nuclear fuel (SNF) and must be managed as waste. The SNF is composed of a UO_2 matrix (> 95 %) and other radioactive elements. The latter are very hazardous, making the waste management difficult. Their hazard progressively decreases by natural processes (radioactive decay) leading, after several millions of years, to a total radioactivity that equals the radioactivity of natural uranium [2]. Therefore, it has been proposed that the most appropriate and natural way of managing this waste is to return it to the Earth's crust. For this aim, the generally agreed solution is the burial of the SNF in the so called deep geological disposal of radioactive wastes for a period, at least, as long as the radioactive decay time.

The design of a deep geological repository must avoid the reach of these radionuclides to the biosphere for such a long time, and the best recognized option for this purpose is the use of a multi-barrier system which, in general, involves containing the radioactive waste inside canisters, then a buffer that protects the canisters and, finally the whole system is surrounded by geological natural barriers. Despite the barriers, it is well-known that, at such a long time, water could be the vehicle that interacts with the barriers and could mobilize radionuclides. Therefore, the studies about the reaction between SNF and groundwater under the possible repository conditions are of great interest [3].

Although the groundwater conditions in a repository are generally reducing, in a layer near the fuel surface, i.e. within < 50 μm of the fuel surface, an oxidative environment has been postulated [4]. This ambient is produced by the radiolysis of

water due to the ionizing radiation associated with the fuel [5-7]. The radiolysis of groundwater results in the production of oxidants as H_2O_2 among others [8], which in contact with UO_2, leads to the formation of uranyl peroxides [9-14]. Studtite: $(UO_2)(O_2) \cdot 4H_2O$, and its dehydration product metastudtite: $(UO_2)(O_2) \cdot 2H_2O$, are the only known uranyl peroxides [15-17] and both were found as corrosion products of SNF [12-14] in two-year experiments with deionized water.

From this foundings, different essays have been performed highlighting that studtite plays an important role in the SNF corrosion process. For example, Amme [18] showed the precipitation of studtite by direct leaching of UO_2 with H_2O_2, and Kubatko et al. [15] showed that studtite may be formed even at very low peroxide concentrations ($1.1 \cdot 10^{-14}$ M H_2O_2), created by the alpha flux of natural uranium ores. Forbes et al. [19] found that studtite could be the alteration product of other uranyl hydrates as schoepite and soddyite, recognized as the fundamental secondary phases of SNF. Furthermore, studtite has been recently proposed as a corrosion product in sea water after the Fukushima-Daiichi nuclear plant accident [20-22]. Despite the importance of this uranyl mineral, there is still some doubt concerning its formation process and crystal structure [17].

The structures of uranyl peroxide hydrates have been investigated by means of theoretical methods in several previous works. The first study was that of Ostanin and Zeller [23] in which the structures of studtite and metastudtite were determined by means of density functional theory (DFT) methods using ultrasoft pseudopotentials. Studtite and the incorporation of neptunium into its structure were later investigated by Shuller [24] using the same kind of techniques and pseudopotentials. These calculations were refined by Weck et al. [25, 26] by using DFT techniques and the projector augmented wave (PAW) method to describe the interaction between valence electrons

and ionic cores. These authors also researched the mechanical stablility of uranyl peroxide hydrates. Walshe et al. [27] have studied the local electronic structure of the hydrated uranium peroxides by means of *ab initio* quantum chemical calculations based on the real space Green function calculations. Studies of atomic clusters closely related to these systems have been reported by Odoh et al. [28, 29].

In this work we study the structure of synthetic studtite by both experimental techniques (SEM, TGA, XRD and Raman spectroscopy) and computational density functional theory calculations. The DFT results were obtained by using a norm-conserving relativistic pseudopotential for uranium atom reported and validated for this kind of materials in a previous work [30]. As far as we know, there is not any published theoretical study on the vibrational spectra of these materials. Comparison of the experimental and computed Raman spectra allows us to assign the different Raman bands that form the whole spectra. The thermal stability of studtite has been analyzed at different conditions by *in situ* Raman spectroscopy. Specifically, we have studied the effect of the heating rate and the presence of liquid water on the studtite irreversible dehydration of studtite.

2. Materials and methods

2.1. Experimental

Synthetic studtite, $UO_2(O_2)\cdot 4H_2O$, was precipitated at room temperature by adding dropwise a solution of 1M H_2O_2 (Sigma-Aldrich) over a solution of 10^{-4} M uranyl nitrate hexahydrate $UO_2(NO_3)_2\cdot 6H_2O$ (Sigma-Aldrich). This reaction yields yellow crystals, which were rinsed with cold water and dried before experiments. The precipitated was characterized by thermogravimetry (TG), scanning electron microscopy (SEM), X-ray diffraction (XRD) and Raman spectroscopy (RS).

A Q50 thermo-balance (TA Instruments, Spain) was used in synthetic air for the TG analysis. Texture of the sample was analyzed with a Jeol 5600-LV scanning electron microscope (SEM) equipped with an Oxford Industries INCA X-sight energy dispersive X-ray spectrometer. XRD was conducted using a Philips PANalytical X'Pert MPD diffractometer using Cu K_{α_1} radiation (λ=1.54056 Å) and operating at 45 kV and 40 mA. A Bragg–Brentano configuration geometry was used. The 2θ range covered was from 20° to 120°, with a scanning step of 0.02° and an overall exposure time of 18 hours. Horiba LabRam HR evolution spectrometer (Jobin Yvon Technology) was used in order to acquire the Raman spectra. A red laser of HeNe with a wavelength of 632.81 nm and a nominal power of 20 mW was used as excitation source. The grating used has 600 grooves/mm leading to a resolution better than 1 cm^{-1}/pixel. The details of this equipment are described elsewhere [31].

In situ Raman characterization of the dehydration of studtite was carried out by using a Linkam temperature controlled pressure stage, THMS-600, coupled with the BX4 Olympus microscope of the Raman spectrometer. The mechanical design and electronics of the Linkam stage provided precise control and temperature stability better than 0.2 K. Spectra were collected with a 50x long-range objective through a silica window (used in place of the standard quartz optical window) on the top of the stage.

A very simple home cell had been specifically used to perform the *in situ* Raman measurements of studtite in contact with liquid water. This cell was mainly composed by two borosilicate glass cover slides separated by an O-ring. Therefore, the sample with water was housed between the two cover slides, separated by the O-ring. A detailed description of this cell and its set up can be found in the Appendix A of the Supplementary Information.

2.2. Theoretical DFT calculations

Studtite models of unit cells have been calculated using the CASTEP code [32], a module of the Materials Studio package [33]. The generalized gradient approximation (GGA) together with PBE functional [34] was used. Grimme empirical dispersion correction, the DFT-D2 approach [35] was used in order to describe properly the hydrogen bonding present in the system studied in this work. Geometry optimization was carried out using the Broyden–Fletcher–Goldfarb–Shanno optimization scheme [36, 37] with a convergence threshold on atomic forces of 0.01 eV/Å. The different kinetic energy cutoffs and k-point meshes [38], must be adopted to ensure good convergence for computed structures and energies. Studtite structure was optimized in calculations with increasing complexity by increasing these parameters. The optimization performed with a cutoff of 1000 eV and a K mesh of 2 x 4 x 4 (8 K points) gave a well converged structure and was used to determine the final results.

For the calculations of vibrational properties, the linear response density functional perturbation theory (DFPT) [39-41] implemented in the CASTEP code was used, where the phonon frequencies at the gamma point of the Brillouin zone were computed using atomic displacement perturbations. Raman intensities are third-order derivatives of total energy with respect to vibrational mode (atomic position) and laser field (electric field, twice). These are calculated in CASTEP [42] by using a combination of perturbation theory (second derivative with respect to field) and finite differences (third derivative with respect to atomic displacement). The frequencies presented in this work have not been scaled to correct for anharmonicity and remaining errors of the theoretical treatment employed, such as incomplete treatment of electron correlation and basis set

truncation [43]. They correspond to the harmonic approximation of the force field. Since the effects of these defects tend to cancel out, the scale factor should be near to unity.

The pseudopotential for uranium atom used is a scalar relativistic GGA-PBE Troullier-Martins [44] type norm-conserving pseudopotential. Its generation was described in a previous work [30].

3. Results and discussion

3.1. Experimental characterization

The synthesized studtite was analyzed by different techniques: scanning electron microscopy (SEM), TGA, X-Ray diffraction (XRD) and Raman spectroscopy (RS). Results are shown in Fig. 1.
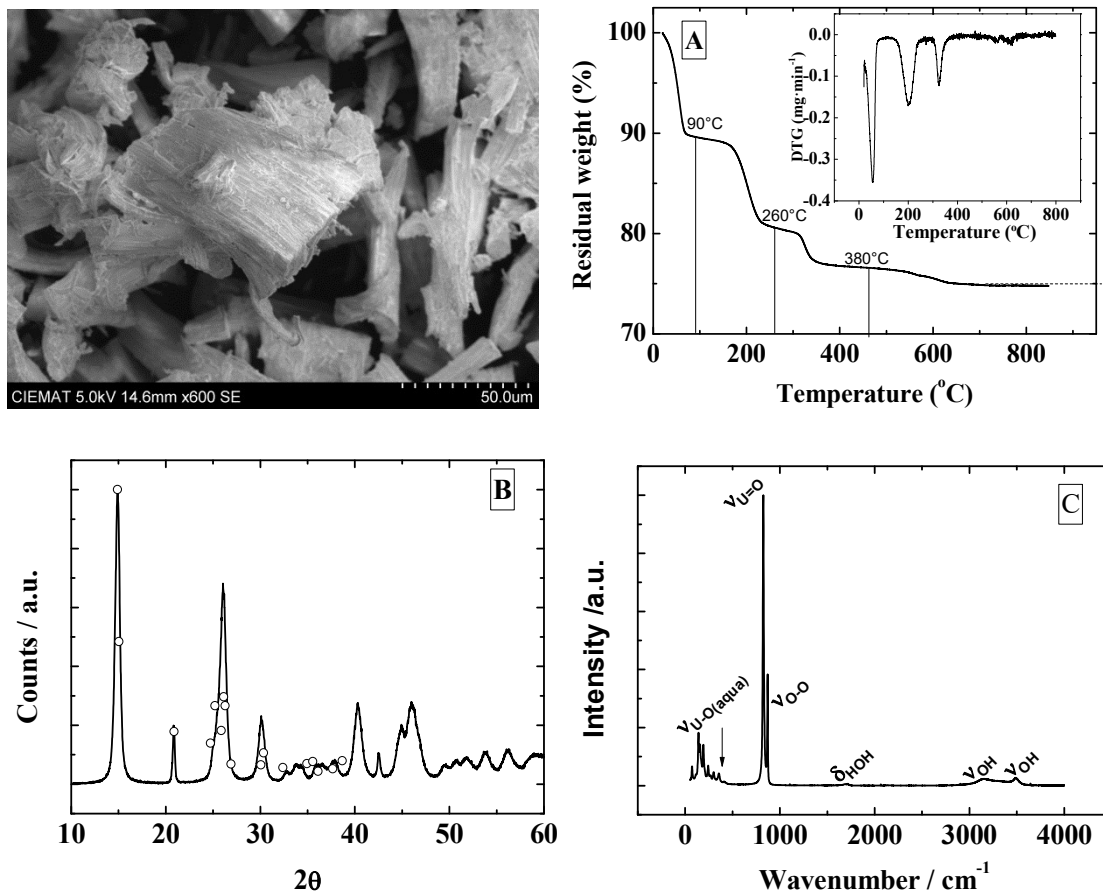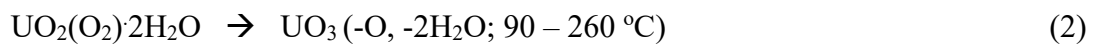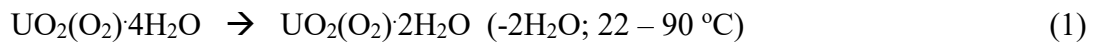
Fig. 1. Synthetic studtite characterization: SEM image of the precipitated crystals, and graphics corresponding to: (A) TGA curve and DTG (thermogravimetric derivative curve), (B) X-ray powder diffraction pattern and (C) Raman spectrum.

SEM micrographs reveal the high crystallinity of the rod-shaped sample, as the general morphology of studtite.

The curve shown in Fig. 1.A was obtained by placing a few milligrams (~ 8 mg) of the sample in the platinum TGA balance, and increasing the temperature up to 850 °C at a rate of 5 °C/min, in a synthetic air flow of 60 mL/min. The TGA results, (see the DTG curve in the inset of Fig. 1.A) show a reasonable agreement with the literature data [45], *i.e.* the initial studtite loses two molecules of water from 22 to 90 °C (Eq. 1). Between 90 and 260 °C the decrease in weight can be associated with a loss of one oxygen and two molecules of water forming UO_3 (Eq. 2), which is not stable and forms U_3O_8 (Eq. 3) at temperatures higher than 570 °C.

$$UO_2(O_2)^.4H_2O \;\rightarrow\; UO_2(O_2)^.2H_2O \;\; (-2H_2O; 22 - 90\ ^oC) \tag{1}$$

$$UO_2(O_2)^.2H_2O \;\rightarrow\; UO_3 \,(-O, -2H_2O; 90 - 260\ ^oC) \tag{2}$$

$$UO_3 \;\rightarrow\; U_3O_8 \tag{3}$$

The XRD pattern showed in Fig. 1.B can be identified as that of studtite [46, 47], $UO_2(O_2)^.4H_2O$, in agreement with the data published by the International Center of Diffraction Data [48], (open symbols in Fig. 1.B correspond to the ICDD 98-016-7992 of studtite pattern).

The Raman spectrum of the sample, shown in Fig. 1.C, corresponds to the typical spectrum of studtite in agreement with the published ones [27, 49, 50]. The only band assignment so far, was performed by Bastians et al. [49] and therefore, in the following

discussion we have used the band assignment given in this reference. Four regions can be distinguished in the spectrum. From 3000 to 3600 cm^{-1} two broad bands are assigned to the OH stretching vibrations of water. Around 1600 cm^{-1} the two small bands are assigned to the water bending vibrations. The strongest bands appear in the intermediate region, from 700 to 900 cm^{-1}. The one at 819 cm^{-1} corresponds to the symmetric uranyl stretch, $\nu^s(UO_2^{2+})$, and the one at 865 cm^{-1} to the peroxo stretch, $\nu(OO)$, of the bridging peroxo ligands. The band at about 348 cm^{-1} was assigned to a symmetric stretching, $\nu^s(UO_{aqua})$.

In Fig. 2 the experimental analysis of the spectrum is presented. The fit, shown in this figure (dashed line), was obtained as follows: first, determining the number of contributions of a given band from the experimental spectrum by the second derivate method; and second, performing a Lorentzian fit. Results are summarized in Table 1, in which they are compared with some published data of this mineral phase [49].
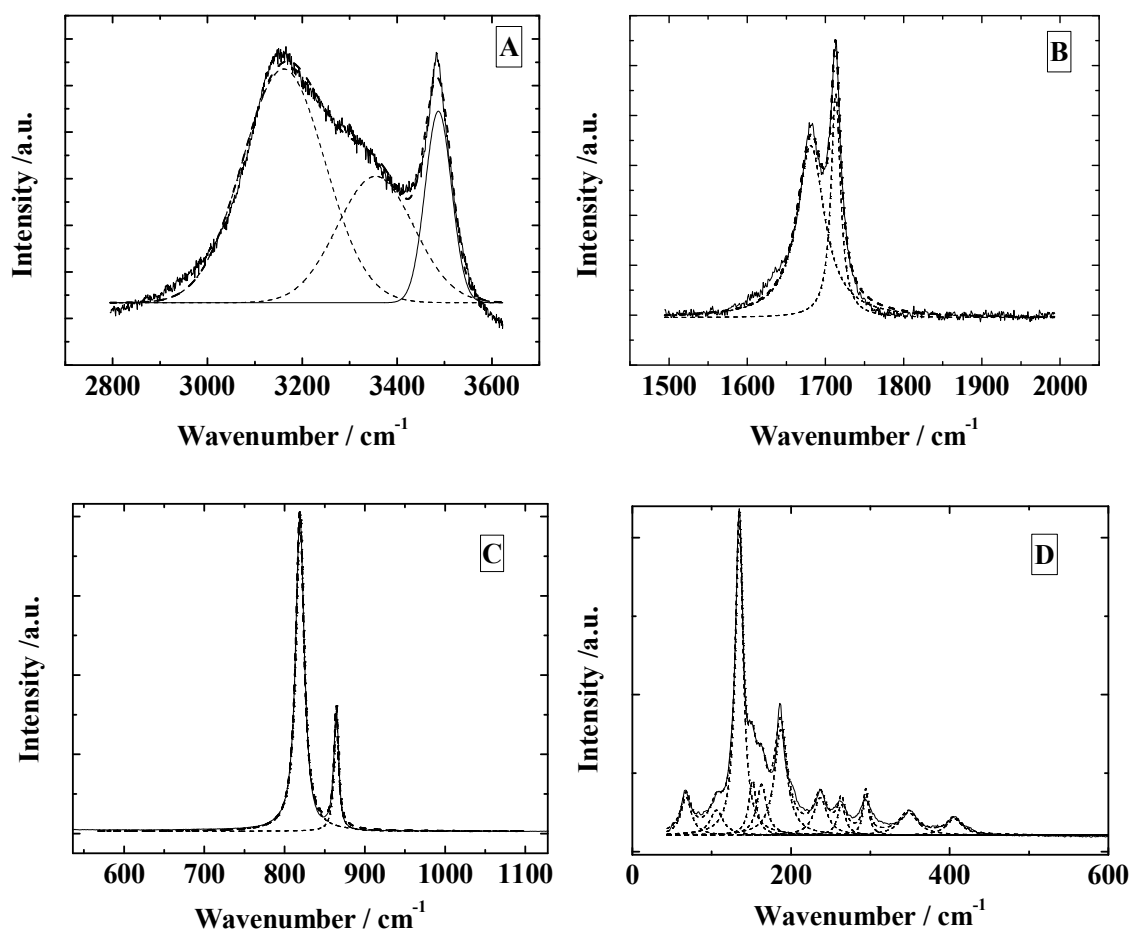
Fig. 2. Experimental Raman spectra obtained for studtite at STP conditions: A) OH stretching region: 2800 - 3600 cm⁻¹, B) OH bending region: 1500 - 2000 cm⁻¹, C) Uranyl and peroxo stretching region: 600 - 1100 cm⁻¹, and D) low frequency region: 50 – 600 cm⁻¹.

Table 1. Raman shift, width and area of the Raman spectrum bands of studtite. Assignments given by Bastians et al. [49] are included for comparison.

Center (cm⁻¹)	Width (cm⁻¹)	Area (a.u²)	Center (cm⁻¹) [49]	Assignment [49]
67.7(0.3)	16(1)	30503(1504)	--	--
106(1)	20 (1)	25115(1220)	--	--
134.61(0.04)	11.8(0.1)	182953(2184)	--	--
151.3(0.4)	11(1)	31312(57111)	--	--

162.8(0.6)	15(2)	37993.0(6203)	--	--
186.9(0.2)	18.9(0.6)	100069(2865)	--	--
236.8 (0.4)	25 (1)	39209 (1461)	238	--
263.4 (0.4)	14.2 (0.8)	16543 (1275)	261	--
294.3 (0.2)	24.5 (0.9)	30935 (1031)	294	--
348.11 (0.8)	33 (1)	27889(1035)	351	$\nu^s(UO_{aqua})$
405.6 (0.9)	29 (1)	18670 (940)	405	--
--	--	--	**433**	--
--	--	--	**815**	--
819.05 (0.02)	12.33 (0.05)	778663 (2133)	819	$\nu^s(UO_2^{2+})$
--	--	--	**840**	--
864.40 (0.03)	6.48 (0.09)	154047 (1491)	864	$\nu(OO)$
1681.1 (0.2)	43.0 (0.7)	116513 (1811)	1648	$\delta(H_2O)$
1713.04 (0.07)	14.6 (0.3)	51439 (1010)	1710	$\delta(H_2O)$
3161(2)	174 (2)	546238 (12150)	3085	$\nu(OH)$
3354 (3)	161 (6)	273672 (14514)	--	--
3487.1 (0.8)	55.6 (0.8)	143344 (3601)	3450	$\nu(OH)$

As can be seen, the data obtained are in good agreement with those previously published, except for the bands at 433, 815 and 840 cm^{-1}. It should be noted that these bands could be due to the presence of impurities, since the bands at 433 and 815 cm^{-1} appear only in the spectrum of the synthetic sample, and they are not present in the natural one. Besides, these bands are very weak. The band at 840 cm^{-1} can be related to metastudtite, and therefore it is probably associated to the partial dehydration of studtite by natural processes or due to heating of the Raman excitation laser.

3.2. DFT calculations

3.2.1. Structure

The optimized studtite structure is displayed in Fig. 3. As can be observed, uranium atom displays hexagonal bipyramid coordination. Two oxygen atoms are in apical positions and the six equatorial oxygen atoms are two peroxo groups (four oxygen atoms) forming opposite edges of the hexagon and two water molecule oxygen atoms. The different bipyramids are linked by sharing the peroxo equatorial edges and form zig-zag chains. The studtite structure has two kinds of water molecules in the structure, one half being the structural ones and the other crystallization water molecules; thus, the structure is more correctly formulated as $[(UO_2)O_2(H_2O)_2] \cdot 2H_2O$. The chains are held together by means of a network of hydrogen bonds between these water molecules. Each water molecule forming part of the uranyl polyhedra (structural water, also called terminal aqua groups) donates two hydrogen bonds with other water molecules which do form part of the bipyramids (crystallization water).
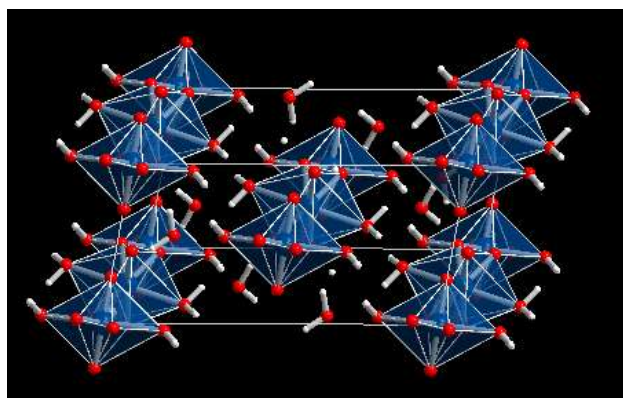

Fig. 3. General view of the studtite structure $(UO_2)(O_2) \cdot 4H_2O$: Color code: U-Blue, O-Red, H-Grey.

The X-ray pattern of studtite was computed from the calculated structure using program REFLEX, a module of Materials Studio Package [33] and compared with an

experimental one in Fig. 4. As can be seen, the agreement in line positions and intensities is quite satisfactory.
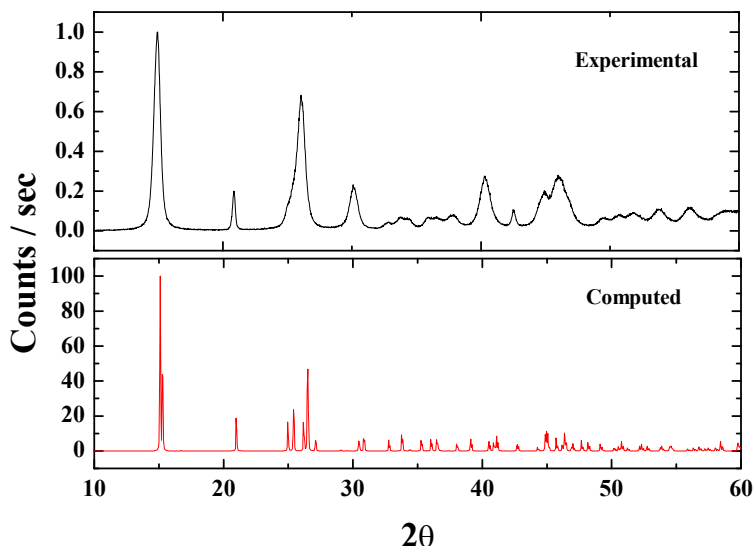

Fig. 4. Comparison of experimental and computed XRD patterns.

Studtite optimized lattice parameters, volumes and densities compared with those obtained in previous theoretical studies [23-26] and experimental results [17] are shown in Table 2. As it can be seen, the agreement is excellent. The computed volume is larger than experimental value by only about 0.7 %. Overstimation of volume and bond distances (see Appendix B of Supplementary Information) is a general trend in DFT calculations [51, 52].

Table 2. Studtite lattice parameters.

Parameters	a (Å)	b (Å)	c (Å)	α	β	γ	Vol. (Å³)	Density (g/cm³)
This work	13.813	6.804	8.496	90.0	122.951	90.0	669.98	3.708
DFT [26]	13.93	6.84	8.55	90.0	122.7	90.0	685.6	-
DFT [24]	13.96	6.88	8.53	90.0	122.55	90.0	689.9	-
Exp. [17]	14.068	6.721	8.428	90	123.356	90	665.6	3.733

A more complete description and additional data about the calculated studtite structure and its X-ray powder spectra is given in Appendix B of Supplementary Information.

3.2.2. *Raman spectrum and band assignment*

The Raman spectrum of studtite was calculated at T=298 K, λ=532 nm, FWHM=5 cm^{-1} and compared with the experimental one in Fig. 5. The experimental and calculated wavenumbers, the calculated intensities and the assignments derived from the calculations are shown in Table 3. The atomic motions associated to each vibrational normal mode are shown in the Appendix C of Supplementary Information.
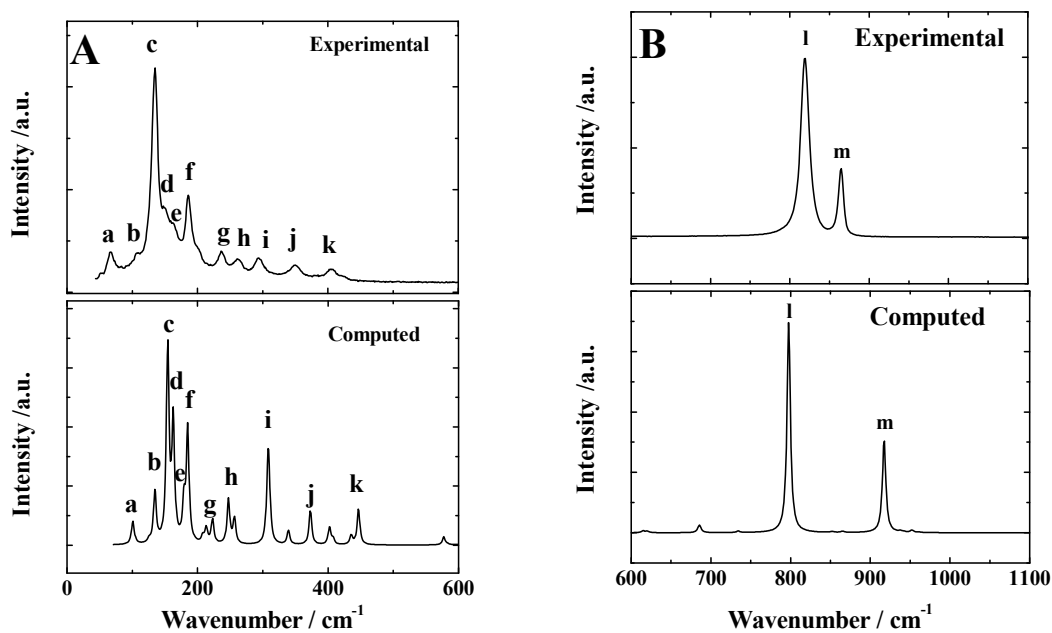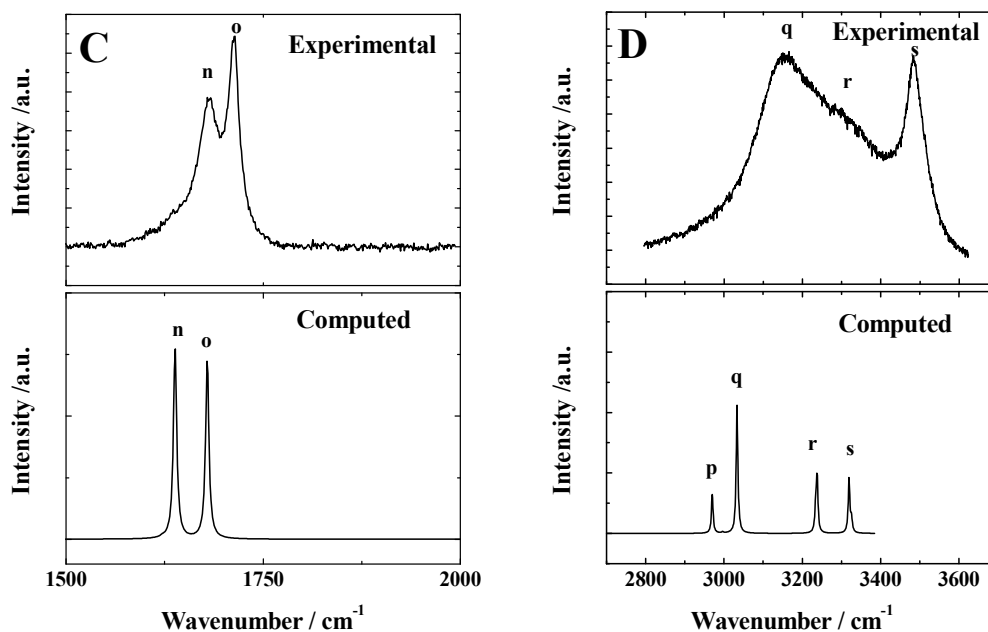
Fig 5. Experimental and computed Raman spectra obtained for studtite at STP conditions: A) Low frequency region: 50 – 600 cm^{-1}, B) Uranyl and peroxo stretching region: 600 - 1100 cm^{-1}, C) HOH bending region: 1500 - 2000 cm^{-1}, and D) OH stretching region: 2800 - 3600 cm^{-1}.

Table 3. Studtite experimental and calculated Raman shifts, calculated intensities and assignations.

Exp. Wavenumber (cm^{-1})	Calc. Wavenumber (cm^{-1})	Irr. Rep. (C$_{2h}$)	Intensity (Å^4)	Assignation
(a)67.7 (0.3)	(a)101	Ag	2.39	$\rho(OUO_{aqua})+\rho(UO_2^{2+})+T(H_2O\text{-cr.})$
(b)106 (1)	(b)135	Ag	9.16	$\rho(OUO_{aqua})+\rho(UO_2^{2+})+T(H_2O\text{-cr.})$
(c)134.61 (0.04)	(c)154	Ag	43.42	$\rho(OUO_{aqua})+\rho(UO_2^{2+})+\rho(OUO_{perox})+T(H_2O\text{-cr.})$
(d)151.3 (0.4)	(d)163	Bg	29.06	$T(H_2O\text{-cr})$
(e)162.8 (0.6)	(e)179	Bg	10.48	$\rho(UO_2^{2+})$
(f)186.9 (0.2)	(f)185	Ag	34.17	$\rho(UO_2^{2+})+\rho(OUO_{aqua})+\rho(OUO_{perox})+T(H_2O\text{-cr.})$
(g) 236.8 (0.4)	(g1)213	Ag	5.66	$\rho(UO_2^{2+})+\rho(OUO_{aqua})+T(H_2O\text{-cr.})$
	(g2)223	Bg	9.864	$\rho(OUO_{aqua})+\rho(UO_2^{2+})+\rho(OUO_{perox})$
(h)263.4 (0.4)	(h$_1$)247	Ag	21.54	$\rho(UO_2^{2+})+\rho(OUO_{aqua})+T(H_2O\text{-cr.})$
	(h$_2$)257	Bg	12.76	$\rho(UO_2^{2+})+\rho(OUO_{aqua})+\rho(OUO_{perox})+T(H_2O\text{-cr.})$
(i)294.3 (0.2)	(i$_1$)308	Ag	40.90	$\rho(OUO_{perox})$
	(i$_2$)309	Ag	32.93	$\rho(OUO_{aqua})+T(H_2O\text{-cr.})$
(j)348.11 (0.8)	(j)373	Bg	30.48	$\rho(OUO_{perox})$
(k)405.6 (0.9)	(k)402	Ag	17.42	$\rho(OUO_{perox})$
(l)819.05 (0.01)	(l)798	Ag	2537.86	$\nu^s(UO_2^{2+})$
(m)864.40 (0.03)	(m)917	Ag	1344.38	$\nu(OO)$
(n)1681.1 (0.2)	(n)1638	Ag	142.66	$\delta(H_2O)$

(o)1713.04 (0.07)	(o)1679	Ag	139.50	$\delta(H_2O)$
(p)----	(p)2970	Ag	2993.29	$\nu(OH)$
(q)3161 (2)	(q)3033	Ag	10233.49	$\nu(OH)$
(r)3354 (3)	(r)3238	Ag	4734.37	$\nu(OH)$
(s)3487.1 (0.8)	(s)3319	Ag	5109.120	$\nu(OH)$

The two bands at the highest wavenumbers are mainly attributed to OH stretching vibrations for the crystallization water molecules and the ones at the lowest wavenumbers to the structural water molecules (see vibrational mode pictures of the Appendix B of Suplementary Information). The two bands placed at about 1650 cm^{-1} represent water bending vibrations, $\delta(H_2O)$. The band at lower wavenumber corresponds mainly to the bending of crystallization water molecules whereas the band at higher wavenumber should be associated to the structural water molecules.

The experimental band at about 864 cm^{-1} is shifted in the computed spectra by nearly 53 cm^{-1} (calculated value is 917 cm^{-1}). It is assigned to peroxo group O-O stretching, $\nu(OO)$. The most intense band in the Raman spectrum appears at 819 cm^{-1} and the calculated wavenumber is 798 cm^{-1}. It is attributed to the uranyl symmetric stretching vibration $\nu^s(UO_2^{2+})$.

The bands placed at 405 and 348 cm^{-1} have theoretical counterparts of 402 and 373 cm^{-1} and are assigned to a $\rho(OUO_{perox})$ vibration. With the symbol ρ we denote an antisymmetric motion of O atoms belonging to equatorial peroxo groups at opposite sides of U atom. Since the O-U-O atoms form an angle of nearly 180 degrees and the central U atom does not move during the motion, the result can be described as a planar rotation similar to a rocking vibration, usually denoted with symbol ρ (see the corresponding vibrational mode pictures in Appendix C of Suplementary information). However, the last band was assigned to an asymmetric U-O$_{aqua}$ stretching, $\nu^{as}(UO_{aqua})$ in the experimental work performed by [49], In this work, the symmetric U-O$_{aqua}$

stretching band appears at a higher wavenumber, at 446 cm^{-1} (see Appendix C of Suplementary Information).

The band located at 294 cm^{-1} is associated with two nearly coincident theoretical bands at 308 and 309 cm^{-1}. The first is assigned to $\rho(OUO_{perox})$. Since in this case the two O atoms of the peroxide group of each side of U atom perform the same vibrations, the peroxide group motion is nearly a translation. The second band is mainly assigned to $\rho(OUO_{aqua})$, that is, now, the O atoms involved are those belonging to equatorial aqua groups. It must be noted that the H atoms in the aqua groups performs similar motions as O atom. Crystallization water molecules nearly translate in this mode.

Bands placed at 263, 184 and 135 cm^{-1} are determined at 257, 185, and 154 cm^{-1}, and attributed to a combination of $\rho(O\text{-}U\text{-}O)$ vibrations, axial $\rho(UO_2^{2+})$ and equatorial $\rho(OUO_{perox})$ and $\rho(OUO_{aqua})$, and crystallization water molecules translations. For the bands at 237, 203, 107 and 67 cm^{-1} we obtained theoretical values of 247, 223, 135, and 101 cm^{-1}, associated with uranyl axial $\rho(UO_2^{2+})$ and equatorial $\rho(OUO_{aqua})$ vibrations and crystallization water molecules translations. Finally, the ones at 164 and 150 cm^{-1} are calculated at 179 and 163 cm^{-1}. The first is assigned to uranyl axial $\rho(UO_2^{2+})$ vibration and the second one to crystallization water molecules translations.

3.3. Thermal stability of studtite

It is well-known that studtite loses two water molecules forming metastudtite with the rise of temperature (see TGA results in Fig. 1.A). In this section the stability of studtite is studied with the aim of knowing the effect of: 1) the heating rate, and 2) the presence of water in the dehydration process.

3.3.1. Heating rate effect

In order to study the heating rate effect on the stability of studtite, different dehydration processes at three different heating rates in dry air were performed in the Linkam stage. The processes were analyzed by *in situ* Raman spectroscopy. Fig. 6 shows, as an example, some of the Raman spectra obtained at different temperatures when a small amount of studtite is heated at 1 ºC/min. Fig. 6.A shows the spectra from 27.1 ºC to 29.6 ºC, Fig. B from 30.2 ºC to 32.6 ºC, Fig. C from 33.2 ºC to 35.6 ºC and Fig. D from 36.2 ºC to 38.7 ºC.
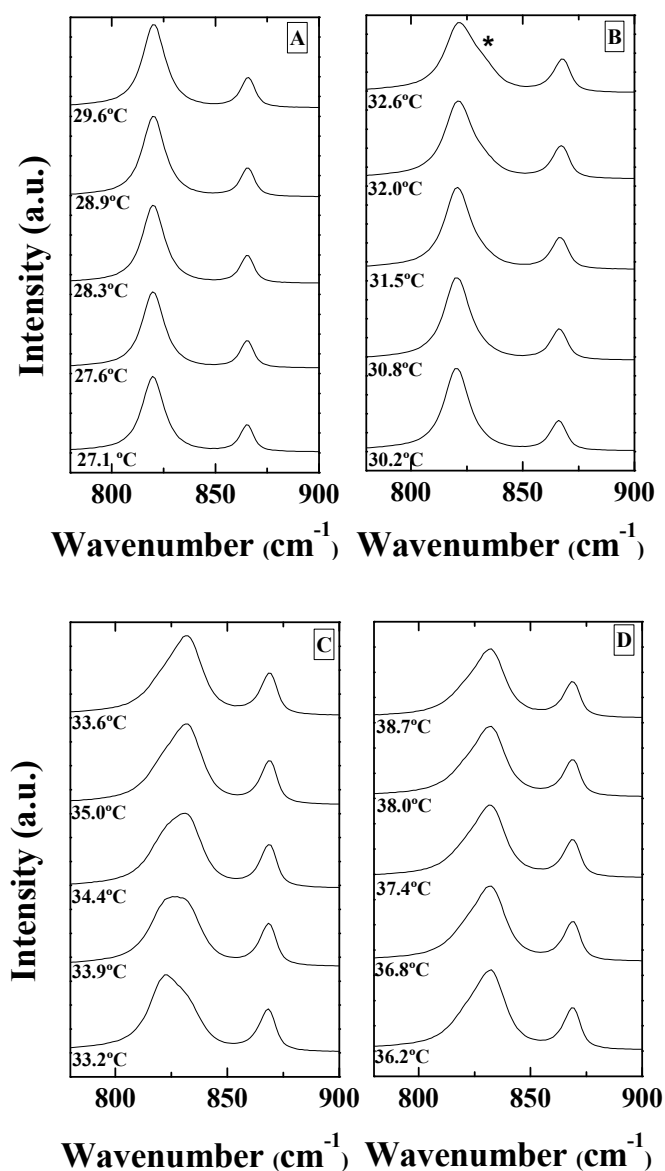
Fig. 6. Evolution of the Raman spectrum along a 1 ºC/min heating process, obtained by the use of Raman microscopy in conjunction with a Linkam thermal stage. Fig. 6.A corresponds to spectra from 27.1 ºC to 29.6 ºC, Fig. B from 30.2 ºC to 32.6 ºC, Fig. C from 33.2 ºC to 35.6 ºC and Fig. D from 36.2 ºC to 38.7 ºC.

As can be appreciated, a new band appears as a shoulder at ~830 cm^{-1} (see asterisk in Fig. 6.B) when the temperature reaches 32.6 ºC. From this temperature on, the intensity of such new band, previously attributed to the metastudtite symmetric uranyl stretch ($v^S_{O=U=O}$) [49], increases. Opposite behaviour is shown for the band corresponding to $v^S_{O=U=O}$ of studtite at ~819 cm^{-1}. At 33.9 ºC the intensity of both bands are very similar, leading to a symmetric broad band centered at ~ 827 cm^{-1}. The intensity of the ($v^S_{O=U=O}$) band corresponding to studtite vanishes at temperatures above 35.6 ºC. In Fig. 6, a shift to higher frequencies of the peroxo stretch v_{O-O} of the bridging peroxo ligands can also be observed at ~ 865 cm^{-1}. This behaviour reflects a phase transition from studtite to metastudtite.

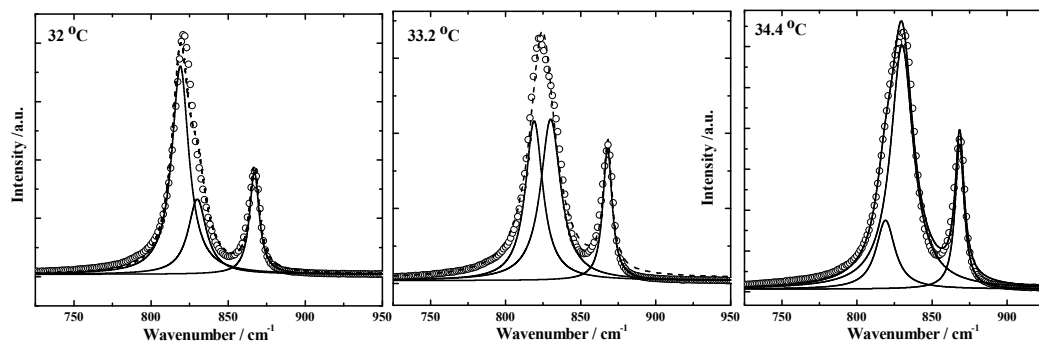Fig. 7 shows the analysis of the Raman spectra obtained at three temperatures in the phase transition region.

Fig. 7. Lorentzian fit of the Raman spectra obtained at three temperatures in the phase transition region.

As can be seen, the band at around ~ 827 cm^{-1} can be understood as the direct sum of the symmetric uranyl stretch ($\nu^S_{O=U=O}$) of studtite (819 cm^{-1}) and metastudtite (830 cm^{-1}).

From this analysis, it becomes clear that it is possible to analyze the phase transition by analyzing the intensities of the mentioned bands. Therefore, the relative intensity I_S/I_{MS}, (where I_S and I_{MS} corresponds to the symmetric uranyl stretch ($\nu^S_{O=U=O}$) intensity band for studtite and metastudtite, respectively) are shown in Fig. 8 as a function of temperature for heating rates of 0.2, 1 and 5 ºC/min.
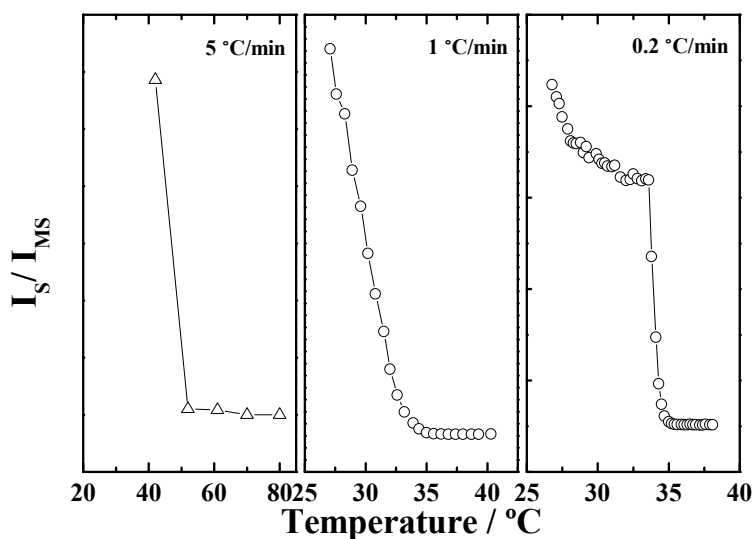
Fig. 8. I_S/I_{MS} ratio as a function of temperature for three different heating rates. I_S and I_{MS} correspond to the symmetric uranyl stretch ($\nu^S_{O=U=O}$) intensity band for studtite and metastudtite, respectively.

By considering the temperature at which the $I_S/I_{MS} \sim 0$, the transition temperatures, T_t, are 50, 35 and 35 °C for the rate studies; *i.e.,* at low heating rates (0.2 °C/min) the transition temperature is around 35 °C, whereas at a high rate (5 °C/min) the T_t is higher. This increase in T_t could be due to the fact that the system is out of equilibrium at such a high heating rate and, therefore, T_t at equilibrium should be obtained in experiments at heating rates below 1 °C/min.

3.3.2. *Presence of liquid water*

The effect of water molecules in contact with the mineral on the studtite thermal stability was studied by placing a few mg of studtite covered with liquid water in the designed cell. The cell was housed in the Linkam stage in which the temperature of the system was increased at 0.2 °C/min. Fig. 9 shows some of the Raman spectra obtained in the *in situ* analysis of these experiments.
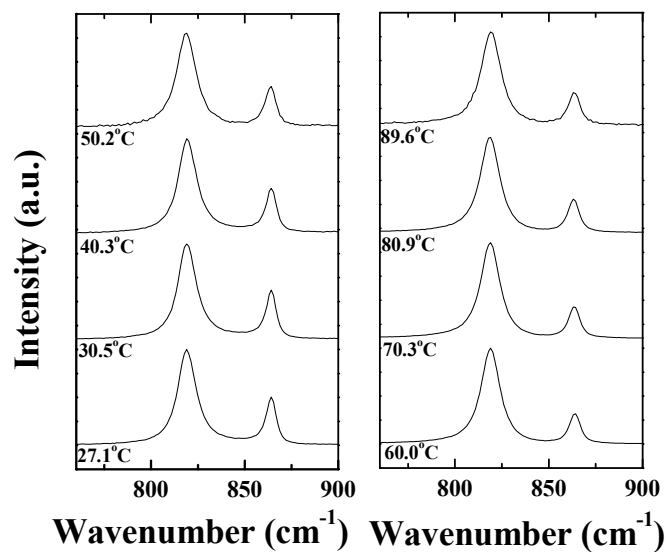
Fig. 9. Evolution of the Raman spectrum of studtite in contact with liquid water during heating experiments in the designed cell with a Linkam thermal stage.

As can be observed, all spectra correspond to the studtite structure, *i.e.,* in presence of liquid water the dehydration of the molecule does not take place in the temperature range studied. This behavior (higher thermal stability against dehydration than that in air) has been shown in other systems [53].

4. Conclusions

In this work studtite was synthetized and characterized by scanning electron microscopy (SEM), TGA, X-Ray diffraction (XRD) and Raman spectroscopy. The structure was besides analyzed by computed DFT calculations. The computed X-ray diffractogram, in agreement with the experimental one, indicates that the optimized structure of studtite describes accurately the experimental studtite structure. Moreover, the computed Raman spectrum shows a correspondence to the experimental bands and, therefore, they could be assigned to specific vibrational motions. The OH stretching and bending bands were found to be associated to specific types of water molecules (crystallization and structural).

The thermal stability of studtite was studied by *in situ* Raman spectroscopy, performing the dehydration of studtite at different heating rates (5, 1 and 0.2 ºC/min) and in presence of water. For this work, a new cell was designed. The results show how the temperature of the dehydration process at low heating rates takes place around 33-34 ºC. However, when the experiments were performed at a higher heating rate (5 ºC/min) the temperature increased at 50ºC. This discrepancy may be due to the fact that the system is out of equilibrium at such a high heating rate, which would explain the TGA

results, and the previous published ones, which shows a high loss of water at low temperatures (< 90 ºC), and points out the importance of applying low heating rates in this kind of studies.

From the experiments performed in presence of water, the studtite is stable up to 90 ºC, what is consistent with the founding of this phase after the Fukushima-Daiichi accident [20-22]. More studies are needed to be done in order to clarify the moisture effect on the thermal stability of this mineral phase.

SUPPLEMENTARY DATA

Supplementary data associated with this article contain two appendices to the present article. Appendix B provides additional details on the theoretical DFT calculations reported in this work. Appendix C gives graphical pictures of the Raman normal modes of studtite.

References

[1] G. Choppin, J.O. Liljenzin, J. Rydberg, Radiochemistry and Nuclear Chemistry, Reed Educational and Professional Publishing Ltd, Oxford, 1995.

[2] A. Hedin, Spent Nuclear Fuel – How Dangerous Is It?. SKB Technical Report 97-13, Swedish Nuclear Fuel and Waste Management Co., 1997.

[3] SKB-91, Final Disposal of spent nuclear fuel. Importance of the bedrock for safety. SKB Report 92-20., 1992.

[4] H. Christensen, S. Sunder, An evaluation of water layer thickness effective in the oxidation of UO_2 fuel due to radiolysis of water, J. Nucl. Mater., 238 (1996) 70-77.

[5] D.W. Shoesmith, Fuel corrosion processes under waste disposal conditions, J. Nucl. Mater., 282 (2000) 1-31.

[6] S. Sunder, Calculation of radiation dose rates in a water layer in contact with used CANDU UO_2 fuel, Nucl. Tech., 122 (1998) 211-221.

[7] A.O. Allen, The Radiation Chemistry of Water and Aqueous Solutions, D. Van Nostrand Co. Inc, Princeton, 1961.

[8] R. Wang, Y.B. Katayama, Dissolution mechanisms for UO_2 and spent fuel, Nucl. Chem. Waste Manage., 3 (1982) 83-90.

[9] G. Sattonnay, C. Ardois, C. Corbel, J.F. Lucchini, M.F. Barthe, F. Garrido, D. Gosset, Alpha-radiolysis effects on UO_2 alteration in water, J. Nucl. Mater., 288 (2001) 11-19.

[10] M. Amme, B. Renker, B. Schmid, M.P. Feth, H. Bertagnolli, W. Döbelin, Raman microspectrometric identification of corrosion products formed on UO_2 nuclear fuel during leaching experiments, J. Nucl. Mater., 306 (2002) 202-212.

[11] F. Clarens, J. de Pablo, I. Díez-Pérez, I. Casas, J. Giménez, M. Rovira, Formation of Studtite during the Oxidative Dissolution of UO_2 by Hydrogen Peroxide: A SFM Study, Envir. Sci. Technol., 38 (2004) 6656-6661.

[12] B. McNamara, E. Buck, B. Hanson, Observation of Studtite and Metastudtite on Spent Fuel, MRS Online Proceedings Library Archive, 757 (2002) II9.7 (6 pages).

[13] B.D. Hanson, B. McNamara, E.C. Buck, F. J.I., E. Jenson, K. Krupka, B.W. Arey, Corrosion of commercial spent nuclear fuel. 1. Formation of studtite and metastudtite, Radiochim. Acta, 93 (2005) 159-168.

[14] B. McNamara, B.D. Hanson, E.C. Buck, C. Soderquist, Corrosion of commercial spent nuclear fuel. 2. Radiochemical analyses of metastudtite and leachates, Radiochim. Acta, 93 (2005) 169-175.

[15] K.-A.H. Kubatko, K.B. Helean, A. Navrotsky, P.C. Burns, Stability of Peroxide-Containing Uranyl Minerals, Science, 302 (2003) 1191-1193.

[16] K.-A. Kubatko, Crystallography, Hyerarchy of cristal structures, and chemical thermodynamics of selectes uranyl phases. PhD Thesis, in: Graduate School of the University of Notre Dame, Illinois, 2005.

[17] P.C. Burns, K.-A. Hughes, Studtite, $[(UO_2)(O_2)(H_2O)_2](H_2O)_2$: The first structure of a peroxide mineral, Am. Mineral., 88 (2003) 1165-1168.

[18] M. Amme, Contrary effects of the water radiolysis product H_2O_2 upon the dissolution of nuclear fuel in natural ground water and deionized water, Radiochim. Acta, 90 (2002) 399-406.

[19] T.Z. Forbes, P. Horan, T. Devine, D. McInnis, P.C. Burns, Alteration of dehydrated schoepite and soddyite to studtite, $[(UO_2)(O_2)(H_2O)_2](H_2O)_2$, Am. Mineral., 96 (2010) 202-206.

[20] C.R. Armstrong, M. Nyman, T. Shvareva, G.E. Sigmon, P.C. Burns, A. Navrotsky, Uranyl peroxide enhanced nuclear fuel corrosion in seawater, Proc. Natl. Acad. Sci. U.S.A., 109 (2012) 1874-1877.

[21] P.C. Burns, R.C. Ewing, A. Navrotsky, Nuclear Fuel in a Reactor Accident, Science, 335 (2012) 1184-1188.

[22] J. Giménez, J. de Pablo, I. Casas, X. Martínez-Lladó, M. Rovira, A. Martínez Torrents, Solubility study and point of zero charge of studtite ($UO_2O_2 \cdot 4H_2O$), Appl. Geochem., 49 (2014) 42-45.

[23] S. Ostanin, P. Zeller, Ab initio study of uranyl peroxides: Electronic factors behind the phase stability, Phys. Rev. B, 75 (2007) 073101.

[24] L.C. Shuller, Atomistic modeling of the solid-state chemistry of actinide materials, PhD Thesis. University of Michigan, 2010.

[25] P.F. Weck, E. Kim, E.C. Buck, On the mechanical stability of uranyl peroxide hydrates: implications for nuclear fuel degradation, RSC Adv., 5 (2015) 79090-79097.

[26] P.F. Weck, E. Kim, C.F. Jove-Colon, D.C. Sassani, Structures of uranyl peroxide hydrates: a first-principles study of studtite and metastudtite, Dalton Trans., 41 (2012) 9748-9752.

[27] A. Walshe, Pru, T. Vitova, R.J. Baker, An EXAFS and HR-XANES study of the uranyl peroxides $[UO_2(\eta^2\text{-}O_2)(H_2O)_2] \cdot nH_2O$ (n = 0, 2) and uranyl (oxy)hydroxide $[(UO_2)_4O(OH)_6] \cdot 6H_2O$, Dalton Trans., 43 (2014) 4400-4407.

[28] S.O. Odoh, G. Schreckenbach, DFT Study of Uranyl Peroxo Complexes with H_2O, F^-, OH^-, $CO3^{2-}$, and NO_3^-, Inorg. Chem., 52 (2013) 5590-5602.

[29] S.O. Odoh, J. Shamblin, C.A. Colla, S. Hickam, H.L. Lobeck, R.A.K. Lopez, T. Olds, J.E.S. Szymanowski, G.E. Sigmon, J. Neuefeind, W.H. Casey, M. Lang, L.

Gagliardi, P.C. Burns, Structure and Reactivity of X-ray Amorphous Uranyl Peroxide, U_2O_7, Inorg. Chem., 55 (2016) 3541-3546.

[30] L.J. Bonales, F. Colmenero, J. Cobos, V. Timon, Spectroscopic Raman characterization of rutherfordine: a combined DFT and experimental study, Phys. Chem. Chem. Phys. 18 (2016) 16575-16584.

[31] L.J. Bonales, C. Menor-Salván, J. Cobos, Study of the alteration products of a natural uraninite by Raman spectroscopy, J. Nucl. Mater., 462 (2015) 296-303.

[32] S.J. Clark, M.D. Segall, C.J. Pickard, P.J. Hasnip, M.I.J. Probert, K. Refson, M.C. Payne, First principles methods using CASTEP, Z. Kristallograph., 220 (2005) 567-570.

[33] MaterialsStudio, http;//accelrys.com/products/materials-studio, (2014).

[34] J.P. Perdew, K. Burke, M. Ernzerhof, Generalized Gradient Approximation Made Simple, Phys. Rev. Lett., 77 (1996) 3865-3868.

[35] S. Grimme, Semiempirical GGA-type density functional constructed with a long-range dispersion correction, J. Comput. Chem., 27 (2006) 1787-1799.

[36] B.G. Pfrommer, M. Côté, S.G. Louie, M.L. Cohen, Relaxation of Crystals with the Quasi-Newton Method, J. Comput. Phys., 131 (1997) 233-240.

[37] M.C. Payne, M.P. Teter, D.C. Allan, T.A. Arias, J.D. Joannopoulos, Iterative minimization techniques for *ab initio* total-energy calculations: molecular dynamics and conjugate gradients, Rev. Mod. Phys., 64 (1992) 1045-1097.

[38] H.J. Monkhorst, J.D. Pack, Special points for Brillouin-zone integrations, Phys. Rev. B, 13 (1976) 5188-5192.

[39] S. Baroni, S. de Gironcoli, A. Dal Corso, P. Giannozzi, Phonons and related crystal properties from density-functional perturbation theory, Rev. Mod. Phys., 73 (2001) 515-562.

[40] X. Gonze, C. Lee, Dynamical matrices, Born effective charges, dielectric permittivity tensors, and interatomic force constants from density-functional perturbation theory, Phys. Rev. B, 55 (1997) 10355-10368.

[41] K. Refson, P.R. Tulip, S.J. Clark, Variational density-functional perturbation theory for dielectrics and lattice dynamics, Phys. Rev. B, 73 (2006) 155114.

[42] V. Milman, K. Refson, S.J. Clark, C.J. Pickard, J.R. Yates, S.P. Gao, P.J. Hasnip, M.I.J. Probert, A. Perlov, M.D. Segall, Electron and vibrational spectroscopies using DFT, plane waves and pseudopotentials: CASTEP implementation, J. Mol. Struct. (Theochem.), 954 (2010) 22-35.

[43] W.J. Hehre, L. Radom, P.V.R. Schleyer, J.A. Pople, Ab Initio Molecular Orbital Theory, Wiley, New York, 1986.

[44] N. Troullier, J.L. Martins, Efficient pseudopotentials for plane-wave calculations, Phys. Rev. B, 43 (1991) 1993-2006.

[45] A. Rey, I. Casas, J. Giménez, J. Quiñones, J. de Pablo, Effect of temperature on studtite stability: Thermogravimetry and differential scanning calorimetry investigations, J. Nucl. Mater., 385 (2009) 467-473.

[46] P.C. Debets, X-ray diffraction data on hydrated uranium peroxide, J. Inorg. Nucl. Chem., 25 (1963) 727-730.

[47] K. Walenta, On Studtite and lts Composition, Am. Mineral. 59 (1974) 166–171.

[48] ICDD, The international center for difracction data. PDF-2 database, (2003).

[49] S. Bastians, G. Crump, W.P. Griffith, R. Withnall, Raspite and studtite: Raman spectra of two unique minerals, J. Raman Spectrosc., 35 (2004) 726-731.

[50] S. Labs, Secondary Uranium Phases of Spent Nuclear Fuel - Coffinite, USiO4, and Studtite, $UO_4 \cdot 4H_2O$ - Synthesis, Characterization, and Investigations Regarding Phase Stability, Forschungszentrum Jülich GmbH Verlag, Zentralbibliothek, 2015.

[51] I. Grinberg, N.J. Ramer, A.M. Rappe, Quantitative criteria for transferable pseudopotentials in density functional theory, Phys. Rev. B, 63 (2001) 201102.

[52] W. Kohn, Y. Meir, D.E. Makarov, van der Waals Energies in Density Functional Theory, Phys. Rev. Lett., 80 (1998) 4153-4156.

[53] I.-M. Chou, R.R. Seal, B.S. Hemingway, Determination of melanterite-rozenite and chalcanthite-bonattite equilibria by humidity measurements at 0.1 MPa, Am. Mineral., 87 (2002) 108-114.